Global System for Atmospheric Modeling: Model Description and Preliminary Results

Marat F. Khairoutdinov[1*], Peter N. Blossey[2], Christopher S. Bretherton[23]

[1]School of Marine and Atmospheric Sciences and Institute for Advanced Computational Science, Stony Brook University, Stony Brook, NY, U.S.A.

[2]Dept. of Atmospheric Sciences, University of Washington, Seattle, WA, USA

[3]Allen Institute for Artificial Intelligence, Seattle, WA

Submitted to

Journal of Advances in Modeling Earth Systems

[*] Corresponding author: Marat Khairoutdinov, marat.khairoutdinov@stonybrook.edu

Abstract

The extension of a cloud-resolving model, the System for Atmospheric Modeling (SAM), to global domains is described. The resulting global model, gSAM, is formulated on a latitude-longitude grid. It uses an anelastic dynamical core with a single reference profile (as in SAM), but its governing equations differ somewhat from other anelastic models. For quasi-hydrostatic flows, they are isomorphic to the primitive equations in pressure coordinates, but with the globally uniform reference pressure playing the role of actual pressure. As a result, gSAM can exactly maintain steady zonally symmetric baroclinic flows that have been specified in pressure coordinates, produces accurate simulations when initialized or nudged with global reanalyses, and has a natural energy conservation equation, despite the drawbacks of using the anelastic system to model global scales. gSAM employs a novel treatment of topography using a type of immersed boundary method, the Quasi-Solid Body Method (QSBM), where the instantaneous flow velocity is forced to stagnate in grid cells inside prescribed terrain. The results of several standard tests designed to evaluate accuracy of global models with and without topography as well as results from real-Earth simulations are presented.

Plain Language Summary

The System for Atmospheric Modeling (SAM), a model widely used to study evolution of clouds and small-scale atmospheric motions using computational grids with horizontal spacings of several meters to a few hundred kilometers, has been extended to simulations of the whole Earth with global grid spacings of 1-5 km that realistically represent intense and localized rain and snow storms. The resulting global atmosphere model, gSAM, is unique in its use of a computationally efficient approximation to the exact equations of air motion and its method of representing flow over mountains, which is well suited to steeply sloped terrain. The paper documents gSAM's updated equations, representation of physical processes, and computational methods. Despite its algorithmic simplicity, gSAM produces realistic global weather forecasts and cloud distributions and agrees well with other more complicated global models on standard benchmarking tests.

Key Points

- The anelastic System for Atmospheric Modeling (SAM) is extended to a global latitude-longitude grid.
- The model uses a novel treatment of topography forcing the flow to instantaneously stagnate in the cells inside prescribed terrain.
- The model performs well in several standard tests that evaluate the accuracy of global models and in real-Earth simulations.

1. Introduction

Global climate change has become one of the most pressing issues of our time and threatens the way of life and even lives themselves of billions of people. Global climate models (GCMs) have been at the forefront of the effort to predict the extent of the future climate change as documented in a steady stream of the IPCC reports (e.g., IPCC 2013; 2021). Although there has been a fair amount of progress on this long and arduous path to the truth, models with parameterized convection have struggled to represent the fundamental feedbacks of the climate system to anthropogenic forcing, particularly the feedbacks associated with clouds (e.g, Randall et al 2003; Stevens and Bony 2013).

One way to further advance our understanding of how the climate system responds to the external influences is to continuously push against the limits of the currently available computer technology by widening the range of resolved scales of atmospheric motion and improving the realism with which physical processes are represented. Even though innovative models that test the limits of present-day computational resources may not be practical for the long simulations required for climate prediction, they may provide us with clues what is wrong with the current generation of the GCMs, and perhaps, even help to improve them. One such innovative models that appeared impractical at first but eventually led to staggering progress in the field of computer modeling of the Earth's general circulation is NICAM (Tomita and Satoh 2004). By using a globe-spanning grid with a spacing of less than 5 kilometers, NICAM was able to explicitly simulate deep convection, thereby becoming the first global storm-resolving model (GSRM). NICAM was so far ahead of its time that several years passed before other models of similar class started to appear. Today, more than a dozen global non-hydrostatic models with 2-5 km grid resolution can run for at least several months at a time.

63 The development of one such GSRM, the global System for Atmospheric Modeling (further
64 gSAM) was motivated by near-global simulations with its predecessor, the original SAM (Khairoutdinov
65 and Randall 2003; further SAM), which is a conventional cloud-resolving model on a Cartesian grid.
66 Those near-global simulations were used to better understand the physics of tropical deep convection and
67 its interactions with the equatorially trapped waves (Bretherton and Khairoutdinov 2015; Narenpitak et al
68 2020), the Madden-Julian Oscillation (Khairoutdinov and Emanuel 2018), and tropical cyclogenesis
69 (Narenpitak et al 2020) within the idealization of an aquaplanet. In those simulations, SAM was applied
70 to tropical convection over very large domains, which are comparably wide as the actual circumference
71 of the Earth. The domain was limited in the latitudinal direction by placing solid walls at about 45^{o} latitude,
72 as further extension using a Cartesian grid would distort the spherical geometry. The walls significantly
73 distort the nearby atmospheric structure and may affect the simulated Hadley circulation throughout the
74 domain.
75 Conceptually, it is straightforward to make SAM a truly global model by replacing its Cartesian
76 grid with a grid based on the spherical coordinates and including simple treatments of terrain and land
77 surface processes. A major technical obstacle was the solver for the global elliptic equation for pressure.
78 SAM uses a fast Fourier transform in both horizontal directions, which works only for Cartesian grids
79 with constant horizontal grid spacing. With colleagues at the Institute for Advanced Computational
80 Science at Stony Brook University, an efficient hybrid FFT-Geometric Multigrid Solver (FFT-GMG),
81 based on Lu (2016), has been implemented in gSAM to address this issue. The terrain is treated using a
82 simple, novel immersed boundary method, unlike in other current GSRMs, which typically use terrain-
83 following coordinates.
84 The first version of gSAM was completed just in time for DYAMOND (DYnamics of the
85 Atmospheric general circulation On Non-hydrostatic Domains; Stevens et al 2019), the first GSRM
86 intercomparison project. DYAMOND was based on a 40-day free run of each GSRM initialized from
87 reanalysis for 1 Aug. 2016 with specified sea-surface temperatures. The gSAM simulation was quite
88 competitive with other GSRMs (Satoh et al 2019; Stevens et al 2019), even though little time was available
89 for model refinement or debugging before the production run. The gSAM is unique among the
90 DYAMOND GSRMs in the formulation of its dynamical core and terrain, and in being developed
91 independent of a major modeling center. It is designed to be an easy-to-use extension of SAM, which
92 itself has a broad user community of cloud-resolving and large eddy simulation modelers.

The purpose of this paper is to formally document gSAM and to report the results of several standard tests of the global dry dynamical core as well as real Earth simulations. The paper is organized as follows. Section 2 describes the model equations, finite-difference approximation, physics packages, implementation of terrain, and numerical methods. Results of several tests of the dry dynamical core and real Earth simulations are presented in Section 3, followed by conclusions in Section 4.

2. Model equations and methods

2.1 Dynamical core

In gSAM, the Cartesian model equations of SAM are reformulated for latitude-longitude coordinates on a sphere by redefining the horizontal metric coordinates x and y as $x = r\lambda$ and $y = r\varphi$, where λ is longitude, φ latitude, and r the Earth's radius. The vertical coordinate is height z. The prognostic anelastic conservation equations for the zonal (u), meridional (v), and vertical (w) wind components, and for mass are:

$$\frac{\partial u}{\partial t} + \frac{1}{\mu}\frac{\partial}{\partial x}uu + \frac{1}{\mu}\frac{\partial}{\partial y}\mu vu + \frac{1}{\bar{\rho}}\frac{\partial}{\partial z}\bar{\rho}wu = -\frac{1}{\mu}\frac{\partial \Phi}{\partial x} + \left(f + \frac{u}{r}tan\varphi\right)v - f^*w + F_u \quad (1)$$

$$\frac{\partial v}{\partial t} + \frac{1}{\mu}\frac{\partial}{\partial x}uv + \frac{1}{\mu}\frac{\partial}{\partial y}\mu vv + \frac{1}{\bar{\rho}}\frac{\partial}{\partial z}\bar{\rho}wv = -\frac{\partial \Phi}{\partial y} - \left(f + \frac{u}{r}tan\varphi\right)u + F_v \quad (2)$$

$$\frac{\partial w}{\partial t} + \frac{1}{\mu}\frac{\partial}{\partial x}uw + \frac{1}{\mu}\frac{\partial}{\partial y}\mu vw + \frac{1}{\bar{\rho}}\frac{\partial}{\partial z}\bar{\rho}ww = -\frac{\partial \Phi}{\partial z} + B + f^*u + F_w \quad (3)$$

$$\frac{1}{\mu}\frac{\partial}{\partial x}u + \frac{1}{\mu}\frac{\partial}{\partial y}\mu v + \frac{1}{\bar{\rho}}\frac{\partial}{\partial z}\bar{\rho}w = 0 \quad (4)$$

where $\mu = cos\varphi$, $f = 2\Omega \sin\varphi$, $f^* = 2\Omega \cos\varphi$, Ω is the Earth's angular velocity of rotation, $\bar{\rho}(z)$ is the prescribed reference density profile, which depends on height only, $\Phi = p'/\bar{\rho}$, where p' is the perturbation of pressure from the reference profile, buoyancy acceleration $B = g\alpha'/\bar{\alpha}$, where g is gravitational acceleration and $\alpha'$is the perturbation of specific volume (inverse density) at the reference pressure from its reference profile $\bar{\alpha}(z)$, F_u, F_v, F_w are accelerations due the subgrid-scale (SGS) eddy viscosity. The pressure-gradient terms in equations (1)-(3) generally follow the kinetic-energy-conserving

version of the anelastic approximation of Lipps and Hemler (1982). The prognostic equation for an arbitrary advected scalar s is given by

$$\frac{\partial s}{\partial t} + \frac{1}{\mu}\frac{\partial}{\partial x} us + \frac{1}{\mu}\frac{\partial}{\partial y}\mu vs + \frac{1}{\bar{\rho}}\frac{\partial}{\partial z}\bar{\rho} ws = S_s + F_s \quad (5)$$

where S_s denotes local sources and sinks, and F_s the divergence of SGS fluxes of s.

2.2 Buoyancy and conservation of energy

For an anelastic model without moist processes, the thermodynamic equation is naturally formulated as prognosis of the potential temperature θ. However, for accurate simulation of moist and radiative processes, the absolute temperature T must also be known (e. g. for calculating the saturation vapor pressure of water). Over regional domains, the reference pressure profile is a good approximation for the pressure field over the entire domain, so the absolute temperature can be estimated from potential temperature using the reference pressure profile (Lipps and Hemler, 1992). However, over a global domain, the local pressure can differ from the reference pressure at the same height by as much as 10%, especially in the middle and upper troposphere. For a given potential temperature, this could change the implied absolute temperature by as much as 10 K, which is far too inaccurate for calculating moist thermodynamics.

Thus gSAM uses a different approach, following Pauluis (2008), who replaced conservation of potential temperature by conservation of frozen moist static energy $h_f = c_p T + gz + L_c q_v - L_f q_{ice}$ (the sum of moist enthalpy and geopotential energy), where c_p is the specific heat of air, L_c, L_s and $L_f = L_s - L_c$ are the latent heats of vaporization, sublimation, and freezing, q_v is water vapor mixing ratio, and q_{ice} is the frozen water mixing ratio. This approximation can be consistently derived from the conservation of moist entropy by replacing the total pressure with the reference pressure and justified by the scaling assumptions used to derive the anelastic approximation. In this same spirit, where pressure is required in a moist thermodynamic formula in addition to temperature, gSAM uses the reference pressure rather than the full pressure. While pressure perturbations are neglected in moist thermodynamics here, their impact was explored in an anelastic framework by Kurowski et al (2013).

In a height-coordinate model like gSAM, the conservation equation for frozen moist static energy involves tendencies of T and q, natural choices for accurately formulating moist thermodynamics, rather

than θ. Like SAM, gSAM is formulated in terms of a liquid/ice water static energy $h_L = h_f - L_c(q_v + q_{liq} + q_{ice}) = c_p T + gz - L_c q_{liq} - L_s q_{ice}$, where q_{liq} is the total liquid water mixing ratio. Like frozen moist static energy, h_L is conserved in nearly hydrostatic air motions even with reversible phase transitions between water vapor, liquid and ice, but it separates off the water contribution to h_f, which is treated in a separate conservation equation. The prognostic equation for h_L is a special case of equation (5) with the source term:

$$S_{h_L} = -\frac{1}{\bar{\rho}}\frac{\partial}{\partial z}(-L_c P_{liq} - L_s P_{ice}) - wB + c_p Q_{rad} \tag{6}$$

Here P_{liq} and P_{ice} are total sedimentation fluxes for liquid and frozen water; Q_{rad} is the radiative heating rate. The buoyancy itself is expressed using absolute temperature as

$$B = g\alpha'/\bar{\alpha} = g((T - \bar{T})/\bar{T} + 0.608 q_v - q_{liq} - q_{ice}) \tag{7}$$

An improvement of gSAM over SAM is the inclusion of the effect of the buoyancy flux wB in (6). As emphasized by Pauluis (2008), it is important to include this term for conservation of total energy, as it opposes the generation/sink of the vertical kinetic energy by the buoyancy. Note that use of temperature, rather than potential temperature, in B differs from the Lipps-Hemler anelastic equations by neglecting the contribution of pressure perturbations to potential temperature perturbations. It is consistent with approximating the total pressure with the reference pressure in the dynamical equations, which requires that buoyancy contributions due to relative horizontal Exner function perturbations $(R/c_p)(p'/\bar{p})$ be much less than those due to relative horizontal temperature perturbations $T'/\bar{T}$. On a global scale, this approximation holds well near the surface but less well in the upper atmosphere; nevertheless, we will see that it does not substantially degrade the accuracy of gSAM in comparison to models that use fully compressible formulations of the flow equations.

The total energy is defined as $E = K + gz + h_f$, that is the sum of kinetic energy K and thermodynamic energy. Similar to Pauluis (2008), it can be shown that the governing equations of gSAM conserve total energy in the whole domain:

$$\frac{\partial}{\partial t}\iiint \bar{\rho} E \, \mu \, dx \, dy \, dz = SHF + LHF - L_f P_{sf} + R_{NET} \tag{8}$$

that is, globally-integrated total energy can only be changed by the total surface flux of frozen moist enthalpy $SHF + LHF - (L_s - L_c)P_{sf}$ and net radiative flux convergence in the atmosphere R_{NET} (=

$R_{SFC} - R_{TOA}$), where SHF, LHF, and P_{sf} are the surface total sensible, latent and frozen precipitation fluxes, respectively; R_{TOA} and R_{SFC} are the top-of-atmosphere and surface net radiative fluxes.

2.3 Consistency with primitive equations in pressure coordinates

For quasi-hydrostatic flows (when horizontal scale of motions is much larger than the vertical), the system of anelastic equations (1)-(4) with thermodynamic equation (6) and buoyancy in form (7) is isomorphic to the system of primitive equations used by many GCMs. Assuming that the reference state is in hydrostatic balance, that is $d\bar{p} = -g\bar{\rho}dz$, defining pressure vertical velocity $\omega = -g\bar{\rho}w$, using the dry expression for buoyancy based on equation (7), neglecting terms with f^*, and neglecting the vertical acceleration, the dry system of equations (1)-(4) and (7) can be rewritten, using the horizontal Cartesian coordinates for clarity, as

$$\frac{\partial u}{\partial t} + u\frac{\partial u}{\partial x} + v\frac{\partial u}{\partial y} + \omega\frac{\partial u}{\partial \bar{p}} = -\frac{\partial \Phi}{\partial x} + fv \tag{9}$$

$$\frac{\partial v}{\partial t} + u\frac{\partial v}{\partial x} + v\frac{\partial v}{\partial y} + \omega\frac{\partial v}{\partial \bar{p}} = -\frac{\partial \Phi}{\partial y} - fu \tag{10}$$

$$0 = -\frac{\partial(\Phi + gz)}{\partial \bar{p}} - \frac{RT}{\bar{p}} \tag{11}$$

$$\frac{\partial u}{\partial x} + \frac{\partial v}{\partial y} + \frac{\partial \omega}{\partial \bar{p}} = 0 \tag{12}$$

$$\frac{\partial T}{\partial t} + u\frac{\partial T}{\partial x} + v\frac{\partial T}{\partial y} + \omega\left(\frac{\partial T}{\partial \bar{p}} + \frac{RT}{c_p\bar{p}}\right) = 0 \tag{13}$$

which is an exact form of the primitive equations (PE) in pressure coordinates based on the reference pressure profile. Note that it is important for the derivation of the system (9)-(13) to have the buoyancy in the form (7) and to include the buoyancy flux term as a source of h_L in equation (6).

The isomorphism of our anelastic system in the hydrostatic limit with the primitive equations can be an advantage both for dynamical reasoning and for initialization from or nudging to a global reanalysis. For instance, the equations of geostrophic balance are the same in both systems (although the interpretation of Φ is slightly different), and thermal wind balance can be expressed very similarly by replacing p by $\bar{p}$ for gSAM, that is, for PE:

$$f\frac{\partial u}{\partial p} = -\frac{\partial}{\partial p}\frac{\partial \Phi}{\partial y} = \frac{R}{p}\frac{\partial T}{\partial y},$$

while in gSAM:

$$f\frac{\partial u}{\partial \bar{p}} = -\frac{\partial}{\partial \bar{p}}\frac{\partial \Phi}{\partial y} = \frac{R}{\bar{p}}\frac{\partial T}{\partial y}.$$

Based on this analogy, a good way to initialize gSAM from reanalysis fields is to interpolate the input data in pressure coordinates to the anelastic reference pressures $\bar{p}(z_k)$ corresponding to the model height levels z_k. A suitable gSAM reference profile $\bar{p}(z)$ is constructed by calculating the globally averaged geopotential height at the reanalysis pressure levels and interpolating this function to obtain the reference pressures at the known heights z_k. The reference density is computed from the hydrostatic balance of the reference pressure profile. This approach will preserve approximate dynamical balances (such as thermal wind balance) in the reanalysis, where they occur.

To illustrate the result of such a procedure, we initialized gSAM with the fields from the ERA5 reanalysis on pressure coordinates at 00Z on January 20, 2020, used for initialization of the most recent DYAMOND-Winter project (https://www.esiwace.eu/services/dyamond-initiative/services-dyamond-winter). We ran gSAM on the same horizontal grid as the ERA5 for one hour to let the fields to adjust to the topography. Then we used gSAM's diagnosed $\Phi = p'/\bar{\rho}$ field to obtain the pressure perturbation of pressure p' which is added to the reference pressure profile to obtain the total pressure field. In Figure 1, the resultant pressure at the surface of the topography is compared to the ERA5 surface pressure. gSAM reproduces the surface pressure quite well, especially over the ocean. Some biases over land are mostly explained by differences in the vertical model grid, topography dataset and interpolation techniques. The difference map clearly shows the imprint of the "staircase" pattern of gSAM surface topography (to be discussed further below) on its surface pressure.

2.4 Physics

Many physics packages in gSAM are directly inherited from SAM. The formulation of the subgrid-scale (SGS) fluxes employs two approaches, the 1.5-order closure based on the prognostic SGS turbulent kinetic energy (TKE) and a simpler Smagorinsky-type closure, used in global simulations, which assumes perfect balance between shear/buoyancy production of TKE and its viscous dissipation. Several microphysics modules are available: the original SAM's single-moment microphysics, and three comprehensive bulk microphysics modules imported from the Weather Research and Forecasting model (WRF): the Morrison et al (2005), Thompson et al (2008), and P3 (Morrison and Milbrandt, 2015). There

are two choices of radiation. The first is from the Community Atmosphere Model version 3 (CAM3; Collins et al 2006), and the second is the Rapid Radiative Transfer Model (RRTM; Iacono et al 2008), from the Community Earth System Model version 1 (Hurrell et al 2013). The former is faster than the latter, but less accurate.

The land surface module is based on the Simplified Land Model (SLM), originally developed for SAM by Lee and Khairoutdinov (2015). There are 16 land types as defined by the International Geosphere-Biosphere Program (IGBP) classification system. Each type defined visible and near-infrared albedos, leaf area index, characteristics of the root system, roughness length and displacement height for surface flux computations, among others. The output of SLM includes land and ice surface sensible and latent heat fluxes, surface albedo for visible and near-infrared radiation, surface skin temperature for longwave radiation, and snow depth. The soil has 9 levels, with thicknesses gradually increasing from 1 cm at the surface to 1 m below. Soil hydraulic and heat conduction properties depend on the clay, sand, and water contents and change sharply if a soil layer is frozen. In addition to soil, SLM computes heat fluxes inside glaciers and sea ice, the depth of which is prescribed from observations. Also, there are parameterizations of accumulation and melting of snow, accumulation of rainwater on tree leaves, surface runoff and flooding. Planned future publications will provide more details on SLM in gSAM. Over the ocean, surface flux and albedo parameterizations from CAM3 are used, as in SAM.

2.5 Numerics

The finite-difference approximations for the equations in gSAM are formulated on Arakawa C-grid, like in SAM, that is, all scalars are defined at the grid-cell centers, while velocity components on grid-cell's sides. Using coordinate transformations, gSAM's model equations can be written and discretized in forms analogous to the Cartesian grid forms used by SAM. By simply setting $\mu = 1$ and $\tan\varphi = 0$ in all the equations, gSAM can seamlessly be switched from a global storm-resolving model to a large-eddy simulation (LES) or a cloud-resolving model (CRM) and thereby include all the functionality of original SAM. gSAM's latitude-longitude grid can also be used for large-area regional modeling where a Cartesian grid would lead to a substantial loss in accuracy. For such regional modeling, gSAM uses strong nudging to the prescribed fields at narrow zones along the domain boundaries.

The advection scheme for all scalars is the fully 3-D monotonic and positive transport MPDATA (Smolarkiewicz 2006), as in SAM. Subgrid-scale fluxes and their divergence, as in equation (5), are

discretized using conventional centered finite differences. Also following SAM, the momentum equations are integrated in time using the explicit third-order Adams-Bashforth (AB3) time scheme. One of the main reasons for using the AB3 scheme is the use of the second order centered difference (SOC) scheme in flux form for advection of momentum with the property of conservation not only of momentum but also of kinetic energy, which also helps to control non-linear instability. The AB3 scheme allows a relatively high maximum Courant number of 0.72 with SOC and is slightly dissipative, which helps to damp the two computational modes inherent in AB3. A disadvantage of AB3 is its strict numerical instability threshold for diffusion $\Delta t < 0.1\, k/\Delta^2$, where k is diffusion coefficient, and Δ is grid spacing. This may cause a serious problem when simulating deep convection and using relatively high vertical resolution in the boundary layer, where relatively large SGS eddy-diffusivity coefficients, predicted by the SGS model, could affect the model stability. AB3 also has also a rather restrictive stability criterion that in Newtonian damping terms, the damping timescale must be longer than about two time-steps (Duran 1991). Therefore, in gSAM, we introduced an additional implicit step for vertical diffusion and damping. The workflow over each time step goes as follows. First, a provisional solution is found using the AB3 scheme as

$$u^* = u^n + \Delta t^n (aA^{n-1} + bA^{n-1} + cA^{n-2}) \tag{14}$$

where A denotes the advection, SGS diffusion (with the exception of the "fast" terms such as the vertical diffusion or strong-damping terms), Coriolis, but not the pressure-gradient terms; a, b, and c are the AB3 coefficients that depend on current Δt^n and past time steps Δt^{n-1} and Δt^{n-2} (Fiedler and Trapp, 1993). Next, a first correction is made to u^* to include vertical diffusion and damping, denoted here by ***B,*** using the implicit step:

$$u^{**} = u^* + \Delta t^n B(u^{**}) \tag{15}$$

Finally, a pressure-correction step is performed to enforce anelastic mass conservation (4):

$$u^{n+1} = u^{**} - \Delta t^n (a\nabla\Phi^n + b\nabla\Phi^{n-1} + c\nabla\Phi^{n-2}) \tag{16}$$

The unknown scaled perturbation pressure Φ^n is diagnosed from the Poisson equation

$$\nabla(\rho\nabla\Phi^n) = \frac{1}{a\Delta t^n}\nabla\cdot\rho u^{**} - \frac{b}{a}\nabla(\rho\nabla\Phi^{n-1}) - \frac{c}{a}\nabla(\rho\nabla\Phi^{n-2}) \tag{17}$$

The procedure above is identical to the time integration of the momentum equations employed by SAM except for the implicit step (15).

The Cartesian grid in SAM has constant horizontal grid spacings in x and y for which the elliptic equation (17) has coefficients that depend only on height; therefore, a bi-directional FFT in the horizontal directions is used to obtain a tridiagonal system of equations for the vertical structure of the horizontal

Fourier coefficients. An inverse bi-directional FFT of their solutions yields Φ^n. This direct method of solving (17) is non-iterative and can be efficiently parallelized across many computational cores.

For the latitude-longitude grid employed by gSAM, the coefficients of equation (17) also depend on latitude, so the bi-directional FFT method can no longer be applied. However, in the usual case that the horizontal grid spacing in the longitudinal direction is constant for each latitudinal circle, none of the coefficients depend on longitude. Then an FFT can still be applied in that direction, yielding a set of independent two-dimensional (latitude-height) Helmholtz equations for the longitudinal Fourier coefficients that can be solved in parallel. For gSAM, the height-latitude grid is highly anisotropic, with thousands of grid cells in the latitudinal direction and only in the order of a hundred in the vertical. In addition, the vertical grid is generally much finer, at least in the low troposphere, than the horizontal grid. Attempts to use freely available generic multigrid solvers have failed because of very low convergence rates for such anisotropic grids with Neuman boundary conditions which would make gSAM too expensive to be practical. Therefore, a custom geometric multi-grid (GMG) solver for anisotropic 2-D Helmholtz equations has been developed (Lu 2016). The resultant hybrid FFT-GMG solver is nearly as efficient as the original bi-directional FFT solver when applied on a grid of similar size. When Cartesian coordinates are used in gSAM, the conventional non-iterative bi-directional FFT solver is still used.

Because of the latitude-longitude grid, the equations have a singularity at the pole. In the early development version of gSAM that participated in the DYAMOND project, this problem was circumvented by placing a solid wall around each of the poles at about 89^o latitude circle. In the current version of gSAM, the grid goes all the way to the poles, so that the horizontal face of the cells in the last row of the grid cells has a triangular shape because the poleward face of otherwise quadrilateral cells degenerates into a point, so the corresponding fluxes, computed on C-grid, through that face are identically zero. The other faces of the polar cells don't have the singularity problem. For other terms, such as Coriolis, when the velocity at the pole is required, the nearest point with valid value of meridional velocity is used instead. To minimize considerable reduction of the timestep because of potentially high CFL numbers in the zonal direction right near the pole, the artificial damping of the horizontal velocity is performed to prevent the CFL from exceeding the critical value. This, of course can distort the solution right near the poles. This problem will be mitigated in the future by using local grid coarsening for the advection in zonal direction (e.g., Asaithambi and Mahesh 2017).

One of the benefits of not using the FFT transform in the *y* direction on latitude-longitude grid is that the grid spacing in *y* can be variable. By varying grid spacing with latitude, the local (in meters, not

in degrees) in y can be the same as resolution in x, effectively covering most of the Earth with a grid that is locally isotropic in the horizontal but has a somewhat broader grid spacing in the tropics than in the midlatitudes. In practice, such a grid is used only to about 70° latitude, and further refinements in y are avoided when approaching the poles, for stability reasons. Such an approach provides about twice as high resolution in midlatitudes than over the equator using the same number of latitudinal grid circles as would be used for a uniformly spaced grid.

2.6 Terrain

A global model without representation of topography would be of little utility beyond idealized aqua-planet studies. Note that SAM has no capability to represent topography. One of the most popular methods for incorporating terrain in atmospheric models is to use a terrain following coordinate system. However, this would mean abandoning both the bi-directional FFT solver for the Poisson equation (17) for pressure in SAM and hybrid FFT-GMG solver in gSAM, replacing them with a fully 3-D multigrid solver. Designing such a solver and making its computational and parallel performance as efficient as the existing solvers in SAM and gSAM would be a very challenging task. Instead, a variant of a so-called body force method has been implemented. In this approach, the velocity of the flow inside a solid obstacle is forced to stagnate, similar to using a fictitious Newtonian damping (Chen and Leach, 2007; Smolarkiewicz et al, 2007). However, we introduce a novel aspect to that approach. We cannot simply set the velocity inside the topography to zero at the end of each time step, as this would violate mass conservation (Eqn. 4). Instead, we damp the flow inside an obstacle using the implicit correction step (15), used before applying the pressure gradient terms, which would look in the case of Newtonian damping with time scale τ as

$$\boldsymbol{u}^{**} = \boldsymbol{u}^{*} - \boldsymbol{u}^{**}\frac{\Delta t^n}{\tau} \tag{18}$$

Step (18) is computationally stable for any value of τ, and can be rewritten as

$$\boldsymbol{u}^{**} = \boldsymbol{u}^{*}\frac{1}{1+\frac{\Delta t^n}{\tau}} \tag{19}$$

For instantaneous relaxation $\tau = 0$, the factor $1/(1 + \Delta t^n/\tau)$ becomes also zero, so that the damping is equivalent to $\boldsymbol{u}^{**} = 0$ inside an obstacle and there is no need to specify a value for τ. The

345 modified $\boldsymbol{u}^{**}$ is used then in the right-hand-side of the Poisson equation (17), solution of which is used to
346 compute the final velocity $\boldsymbol{u}^{n+1}$ for the current time step.

347 The approach, which we called the Quasi-Solid Body Method (QSBM; Khairoutdinov et al 2022),
348 has the virtue of simplicity, as it requires very little change to the model code (and no change to the
349 structure of the Poisson solver), and can, in principle, be adopted by any anelastic model. Moreover, the
350 method works not only for topography, but also buildings. For that case, the method has already been
351 tested by comparing the simulated flow around a single rectangular building to the wind-tunnel
352 observations with good results (Khairoutdinov et al, 2022).

353 There are drawbacks to the QSBM. First, the method does not guarantee that the velocity inside
354 the terrain remains completely stagnant, as some residual flow is unavoidable. However, the magnitude
355 of the residual velocities is found to be very small, typically one to two orders of magnitude smaller than
356 the velocity of the incoming flow, even in the case of a building. The simulation can further be improved
357 by reapplying the QSBM to the solution at the end of the time step, although each such iteration increases
358 the expense of the model because of the repeated use of the elliptic equation solver. Khairoutdinov et al
359 (2021) performed up to three such additional iterations and found that each iteration reduces the residual
360 velocities inside the building further by about a factor of two. For example, for an oncoming wind of
361 several meters per second, the maximum residual flow was only several centimeters per second. However,
362 it was also found that the additional iterations result in only minor simulation improvement compared to
363 the observations, and therefore, can generally be omitted in most cases.

364 Another drawback of the QSBM is that the topography can be represented only by whole grid
365 cells, resulting in "staircase"-like mountain shapes and poor representation of gently sloped terrain.
366 Therefore, the method works the best for buildings and very steep terrain. In the past, several methods
367 have been developed to address such a problem, for example the "shaved cells" approach (Adcroft et al.
368 1997). However, such methods would result in an elliptic equation (17) having coefficients that are
369 functions of longitude as well, which prevent the use of an FFT in zonal direction and would require a
370 more complex 3-D multigrid solver.

371 "Staircase" terrain can generate short-wave (two-delta) noise around obstacles. In gSAM, a
372 numerically dissipative third-order upstream-biased scheme (TOB) is used to help to control the small-
373 scale noise around topography. To minimize overdamping by the TOB scheme, the hybrid scheme is
374 employed to compute the momentum advection tendency a weighted superposition of the momentum
375 tendencies due to SOC and TOB schemes. The TOB scheme used together with the AB3 is somewhat less

stable than the SOC scheme, with a maximum stable Courant number of about 0.39 vs 0.72. However, the stability threshold of the hybrid scheme changes almost linearly with the weighting coefficient α between the stability thresholds of the SOC and TOB schemes. Experimentally, using a 1-D advection test, the following empirical relationship between maximum stable Courant number (CFL) and partitioning weight α is found: $CFL = 0.39 + 0.23\alpha + 0.09\alpha^2$. For example, for α=0.7, that is 70% of momentum tendency due to SOC and 30% due to TOB scheme, which is usually sufficient to control the short-wave noise, the maximum stable Courant number is about 0.6, compared to 0.72 if only SOC is used. This reduces the maximum time step required to maintain a stable solution by about 20%.

3. Results

3.1 Steady state test (gradient-wind balance)

To demonstrate that gSAM's anelastic approach indeed gives results equivalent to the primitive equations in pressure coordinates in the hydrostatic limit, as discussed above in Section 2.4, the idealized steady-state case developed by Jablonowski and Williamson (JW06; 2006) is used. The initial conditions in JW06 describe a steady-state rotating atmosphere in the hydrostatic and gradient-wind balance as an analytic solution to the primitive equations. The prescribed structure of the zonally symmetric temperature distribution and corresponding zonal thermal wind are shown in Figs. 2*a-b* and closely resembles the real atmosphere. A perfect model based on the primitive equations should maintain that initial gradient-wind balance indefinitely without developing any instabilities or meridional circulation. For the test, we use a relatively coarse 512x256 horizontal grid (approximately 0.7^o uniform grid spacing) with 30 vertical levels whose spacing gradually reduces from about 100 m near the surface to 5000 m near the domain top at 37 km. This is comparable to the GCM grids used in the JW06 study. The time step is 30 s. As suggested by JW06, no explicit noise damping or SGS diffusion is applied. The non-dissipative SOC scheme is used for advection of momentum. To minimize round-off errors, all computations are done in double precision. Following the discussion in Section 2.3, the specified initial temperature and velocity fields are not interpolated from pressure-sigma to height coordinates; instead, they are interpolated to the reference pressures corresponding to the gSAM height levels, calculated following Sec. 2.3 with the global-mean geopotential height as a function of pressure calculated by integrating the hydrostatic equation vertically with the globally averaged temperature profile and surface pressure prescribed by JW06. This approach

enables gSAM to preserve the initial thermal wind balance of the unperturbed basic state specified in pressure coordinates.

Starting from the prescribed zonal velocity and temperature fields, the model is integrated for 30 days. The resultant zonal wind remains nearly steady, developing slight wind anomalies with the amplitudes of less than about 0.1 m/s even in the region of jets in midlatitudes, as shown for day 30 in Fig. 2*c*. Note that the reference pressure profile is used as the vertical coordinates on these plots. Even smaller errors are found for the meridional wind (not shown). The slight imbalance can be explained by the relatively coarse grid used in this test. As expected, the gSAM initialization procedure and numerics almost precisely maintain the thermal wind balance of the prescribed temperature field and zonal wind, even though they were designed for pressure/sigma-coordinate models. The corresponding geopotential height proxy $\Phi/g + z$ computed by gSAM, shown in Fig. 3d, is nearly identical to the geopotential height prescribed in JW06 (see their Fig. 1e).

3.2 Baroclinic wave test

The zonally symmetric state in the previous test is baroclinically unstable, and baroclinic waves can be triggered from a relatively small-amplitude initial zonal wind perturbation in mid-latitudes as described in JW06. The model is run for 10 days with such an initial perturbation and the same grid as described in the previous test. Snapshots of the surface pressure and of the temperature and vorticity at 850 hPa are shown in Fig. 3. As there is no analytical solution, we compared our results to numerous results from other dynamical cores found in literature, including JW06. Overall, the magnitudes and the shapes of the displayed fields compare quite well with other dynamical cores, with the notable exception of the longitudes of the disturbances, which seem to be advanced forward by about 10^o in gSAM. A similar result was reported by Kurowski et al (2015), who directly compared results from compressible and anelastic versions of the same model, although for a somewhat different moist baroclinic wave test. They attributed that advance to the delayed onset of the rapid growth of the baroclinic wave in their anelastic version of the model. In our case, the initial conditions may also play a role in the apparent phase bias of the baroclinic wave, as the initial wind perturbation specified by JW06 does not satisfy the anelastic continuity equation. As the result, gSAM immediately tries to make the flow non-divergent, reducing the

amplitude of the initial zonal wind perturbation from 1 m/s to 0.5 m/s, and also creating a rather strong perturbation of the meridional wind, which is initially absent.

3.3 Held-Suarez test

Held and Suarez (1994; further HS94) developed a standard test of how well dry dynamical cores simulate statistical properties of mid-latitude baroclinic eddies. The test prescribes highly idealized diabatic heating and cooling as well as the boundary layer damping. The model then runs for very long time to obtain the time-averaged statistics. As there is no analytical solution or observations, the model results are typically compared to the results of other dynamical cores. We run gSAM for 1200 days using a 288x144x30 grid (uniform 1.25^o spacing in latitude and longitude) with the domain top at 37 km and a 20 s time step. The Smagorinsky closure is used for the SGS fluxes, with SOC differences of momentum fluxes. Above 22 km, a sponge layer is used to control vertically propagating gravity waves. The initial state is motionless isothermal atmosphere with the temperature of 300K.

After allowing 200 days for model spin-up, statistics are calculated over the last 1000 days and shown in Fig. 4. Overall, the results agree well, both qualitatively and quantitatively, with the climatology in HS94 as well as other models. For example, Figure 4 compares the zonal wind, meridional eddy-flux of zonal momentum and meridional eddy flux of temperature to the results obtained by CAM with a spectral Eulerian dynamical core (CAM-EUL) running with T85 truncation and 30 levels, comparable in resolution to the grid used by gSAM in this test. The plots for CAM were obtained from its official website https://www.cesm.ucar.edu/models/simpler-models/held-suarez.html. One can see that, in general, gSAM and CAM-EUL agree quite well in the position, structure and strength of the westerlies in midlatitudes and of the easterlies in the tropics and polar regions, as well the meridional eddy fluxes of momentum and heat. The zonally averaged temperature also looks quite similar to HS94 results. A kinetic energy spectrum for midlatitudes shows the canonical k^{-3} power law for the large-scale eddies transitions to a $k^{-5/3}$ power law for relatively short scales, which is consistent with the observed spectra in the real atmosphere in mid-latitudes (e. g. Nastrom and Gage, 1985).

3.4 3-D Rossby-Haurwitz wave

This test is an extension of a standard 2-D test for the shallow water models discussed by Williamson et al (1992). We use the formulation of the 3-D test as described by Jablonowski et al (2008). Despite being formally a 3-D test, the wave itself is essentially a 2-D barotropic wave, propagating westward with a constant speed and preserving its shape. Therefore, it is a very useful test to check the implementation of the Coriolis and metric terms and the ability of the model to maintain such a wave for long time. The domain has 576x288x30 grid points (0.625^o horizontal grid spacing and 30 levels), and time step is set to 30 s. The number of wavelengths around the equator is set to 4, which corresponds to a propagation speed of about -15.2^o per day, or 24 days for the full revolution around the globe, which is the model's integration time in this case. Figure 4 shows zonal and meridional wind components as well as the surface pressure at the end of the run. The propagation speed computed from the Hovmöller diagram (not shown) turned out to be very close to this theoretical value. The shape and magnitude of the simulated fields in Fig 4 are barely different from the initial fields after 24 days of integration.

3.5 Non-hydrostatic mountain waves

The tests presented thus far have dealt with quasi-hydrostatic large-scale flows. The present test examines the non-hydrostatic response of gSAM to flow over the terrain profile proposed in Schär et al (2002; further S02), which prescribes a series of bell-shaped mountains with the tops inside a cosine-like envelope. Two cases are considered, a 2-D mountain range case following S02, who also provided an analytical solution, and a 3-D circular mountain following the case 2.1 from the DCMIP 2012 (Ullrich et al 2012), for which linear analytical solution has also been developed (Klemp et al 2015; further K15). For this test we use gSAM in Cartesian coordinates as our goal here is primarily to test the implementation of the terrain. The atmosphere is isothermal at 300 K, with uniform wind of 20 m/s. The domain has 512x512x80 grid points with 333.3 m grid spacing to make the domain similar in size to the domain in S02, with the top at 37 km. The vertical grid spacing gradually increases with height, from 40 m near the surface, to 500 m at 3600 m, staying constant up to 19 km, and then again monotonically increasing to 1400 m at 37 km. The maximum height of the terrain is 250 m with 5000 m mountain-range half-width and 4000 m mountain wavelength, which represents the distance between individual mountain peaks. This vertical grid is the same one used by gSAM in DYAMOND (Stevens et al, 2019) and was not specially refined for this specific test. As the result, the terrain is represented rather coarsely in the vertical by only 6 grid levels below the highest mountain peak. To avoid reflection of gravity waves from the top of the

domain, a sponge layer is placed above 20 km. Vertical cross-sections of vertical velocity after two hours of simulation are shown in Figs. 6a and 6b for the 2-D and 3-D cases, respectively. Both simulations agree quite well with the analytical solutions Figs. 6c and 6d, which are adopted from K15. There is little evidence of the effect of terrain "staircasing" on the simulation, mostly because of the use of hybrid SOC-TOB momentum advection in the vicinity of the mountain with α=0.7 (see sec. 2.6 for details). There are some additional perturbations compared to the linear analytical solution, probably because of nonlinear effects. Horizontal cross-sections of vertical velocity for 3-D simulation at 8 and 16 km are shown in Figs. 7a and 7b. They also compare quite well to the analytical solutions Figs. 7c and 7d, also adopted from K15.

3.6 Mountain induced Rossby wave train

This is another test of the terrain implementation in gSAM, this time for hydrostatic flow over the globe. The case set-up follows the specifications in the DCMIP 2008 report (Jablonowski et al, 2008). The base state is an isothermal atmosphere in zonally symmetric solid-body rotation, which is constant with height, with maximum wind at the equator of 20 m/s. This base state is perturbed by an idealized bell-shaped 2000-m high mountain, with half-width of 1500 km, centered at 90^{o}E and 30^{o}N. The grid configuration is similar to the Rossby-Haurwitz wave case. To minimize reflection of gravity waves from the model top, a sponge layer in the upper third of the domain is employed. The solution for the zonal and meridional wind components at 700 mb levels at days 5, 15 and 25 are shown in Fig. 8. There is no analytical solution for this case, but the results compare well with those from other models shown in DCMIP report by Jablonowski (2008; Fig. 20) and also by Ullrich and Jablonowski (2012). As noted by the latter, the models in this test usually begin to diverge after 15 simulated days.

3.7 DYAMOND-Winter real Earth simulation

So far, we presented the results of several idealized tests, just a few of many that have been developed over the years. Such idealized tests have been routinely used by the weather and climate modelling communities to identify the problems with models' formulation, their major weaknesses, and for finding "bugs" in their code that would be difficult to find otherwise in realistic simulations, as many of the problems and bugs could be simply hidden in the general clatter and noise of such simulations.

However, gSAM is not a new model per se: it is an extension of the well-established SAM to a global domain. Aside from the topography implementation, the rest of the physics in gSAM is basically identical to SAM's. Therefore, in addition to the tests of the dry dynamical core, cloud-resolving simulations of the real Earth have been also performed and evaluated. Because of the considerable computational cost of such realistic simulations, relatively few of them have been performed to date. The very first such simulation was for the aforementioned DYAMOND project (Stevens et al, 2019), for which the results of gSAM have been quite encouraging. The model has also performed short hindcast simulations using different microphysical schemes during the SOCRATES (Southern Ocean Clouds, Radiation, Aerosol Transport Experimental Study) field experiment, as reported by Atlas et al (2021) whose analysis focused on a comparison of mixed-phase clouds over the Southern Ocean simulated by different microphysical parameterizations implemented in SAM. Recently, gSAM has also participated, among several other GSRMs, in the second phase of the DYAMOND project. Below, we present just a few highlights from that simulation, reserving more substantial discussion and analysis for future publications.

The DYAMOND-Winter simulation covers a 40-day period from January 20th to March 1st, 2020. Initialized from ERA5 reanalysis at 00Z on January 20th, gSAM ran for 40 days using prescribed sea surface temperatures and sea ice cover. The CAM3 radiation and standard SAM's single-moment microphysics are used. The grid has 9216 x 4608 grid cells in the horizontal and 74 levels in the vertical. The grid spacing is locally isotropic in the horizontal (same in both meridional and zonal directions) until about 70^{o}N/S with grid spacing of 4.25 km over the equator, gradually decreasing to 2-3 km in midlatitudes, then coarsening towards the poles to maintain numerical stability. The time step is 10 s.

Figure 9 compares the 5-day average (January 21st to January 25th) of precipitation, surface latent heat flux (LHF), and top-of-atmosphere (TOA) outgoing longwave (OLR) and absorbed solar (ASR) radiative fluxes to ERA5 reanalysis. These five days are used to make a quantitative comparison to reanalysis before the model divergence from the observed state due to natural variability. The first day has been neglected to allow for model spin-up. Overall, the geographic pattern of the mean precipitation is reproduced quite well, and gSAM's global mean precipitation of 3.0 mm/day is similar to the 2.9 mm/day five-day average in ERA5. The most notable bias of gSAM is the relatively light precipitation in the South Pacific Convergence Zone (SPCZ) in tropics. It is encouraging to see orographically enhanced precipitation zones over the southern tip of South America and the Pacific coast of Colombia, as well as over Norway, the Pacific Northwest, and South Africa, implying that gSAM's representation of the topography works reasonably well. The geographic distribution of the surface LHF also compares quite

560 well to ERA5 estimates, with a global mean value of 83.9 W/m^2 in gSAM and 80.0 W/m^2 in ERA5. The
561 performance of gSAM's land model is validated by good agreement with ERA5 for LHF over land,
562 especially over the heavily vegetated areas of tropics and subtropics, where these fluxes vary strongly due
563 to the diurnal cycle and also depend on partitioning of total flux between the evapotranspiration and
564 sensible heat fluxes.

565 The simulated pattern of OLR compares well to ERA5, showing large areas filled with cold cloud
566 tops over tropical land masses, the SPCZ, and major storm-tracks in midlatitudes. In cloud-free areas over
567 subtropical oceans, the OLR tends to be overestimated, but is underestimated over convectively active
568 regions over land in tropics. The overall pattern of the ASR is simulated by gSAM reasonably well, but
569 there are many regional biases, most prominently over the Southern Ocean. Atlas et al (2021) showed that
570 the low bias in ASR over the Southern Ocean seen in Fig. 9d can be removed by using a microphysics
571 scheme in gSAM that more efficiently glaciates supercooled shallow cumuli. Global mean OLR is higher
572 in gSAM than in ERA5, 245.4 W/m^2 vs 240.2 W/m^2, while at the same time, global mean ASR is
573 considerably underestimated in gSAM relative to ERA5, 241.6 W/m^2 vs 248.8 W/m^2. Therefore, the net
574 incoming radiative flux at TOA (ASR-OLR) is -3.8 W/m2 in gSAM vs 8.6 W/m^2 in ERA5, a difference
575 of about 12 W/m^2. While radiative fluxes from ERA5 should not be considered "ground truth", this large
576 discrepancy between gSAM and ERA5 warrants further investigation, including its sensitivity to the
577 choice of radiation and microphysics packages in gSAM.
578
579 *3.8 Hindcast of Hurricane Irma*
580
581 Although weather forecasting was never a motivation for the extension of SAM to a global domain,
582 the ability of gSAM to forecast a tropical cyclone has been tested by performing a hindcast of Hurricane
583 Irma, one of the most powerful Atlantic hurricanes of the 2017 season. Irma reached Category 5,
584 devastated several Caribbean islands, struck Cuba and the Florida Keys, and eventually made landfall in
585 Florida. Global numerical weather prediction models had difficulty forecasting its path. For example, Fig.
586 10a shows a so-called "spaghetti" plot with predicted tracks of Irma as of September 5th, 2017 based on
587 forecasts from several NWP models, approximately 5-6 days before landfall in Florida. One can see a
588 wide spread of the trajectories with no clear indication on which coast of Florida (east or west) Irma would
589 make landfall. After initialization from ERA5 reanalysis at 00Z on September 5, gSAM was run for 7
590 days. After initialization, the sea-surface temperature was not updated since a real forecast model would

not have such information. An ensemble of 10 simulations was made with coarse, 17-km grid spacing using a global 2304x1152 grid, along with one high-resolution deterministic run using 4.25-km spacing using a 9216 x 4608 grid. All runs used 74 vertical levels and a domain top at 37 km, and no cumulus parameterization was employed. The ensemble was used to determine the most probable path of Irma, while the deterministic run was used to make the intensity forecast. All runs were performed on the Cheyenne supercomputer at NCAR using 1152 cores for the ensemble runs and 4608 cores for the deterministic run. Each ensemble member ran about 50 times faster than wall-clock time, while the deterministic simulation ran 6 times faster than wall-clock time. Note that gSAM could run on twice as many processors as this, which would further increase the throughput by about 80%. For a 7-day forecast, each of the ensemble runs (which could be done concurrently) would then take less than 2 wall-clock hours, and the deterministic forecast would take about 16 hours.

Figure 10b compares the predicted tracks of Irma from all runs with the estimated best track from observations. The ensemble generates a wide spread of tracks toward the end of the runs, with the ensemble mean following the actual path of Irma quite well and correctly predicting that Irma would make landfall on the east coast of Florida. Fig 10c shows one "lucky" ensemble member that predicted the actual path of Irma almost perfectly. Figs 10e and 10f show the minimum surface pressure and maximum sustained wind near the surface as well as best-track data. Because of ERA5's rather coarse resolution, the initial depression associated with Irma was relatively weak, so it took several days for the model to properly spin up the hurricane. As expected, 17-km resolution is not sufficient for predicting the minimum pressure and intensity of the hurricane but can be useful for predicting its path. The 4-km deterministic forecast predicts the intensity much better despite not being the best in predicting the hurricane's track. Overall, the results produced by gSAM in this hurricane case are encouragingly realistic given the approximations inherent in gSAM's dynamical equations. This gives a more favorable view of gSAM's ability to simulate tropical cyclones than the DYAMOND analysis of Judt et al. (2021) and shows that gSAM is suitable for both realistic and idealized global simulations requiring storm-resolving grid resolution.

4. Conclusions

This paper describes the extension of the cloud-resolving and large eddy simulation model, SAM, to a global domain. The resulted global storm resolving model, gSAM, is formulated on a latitude-longitude grid but can seamlessly switch back to Cartesian coordinates. Hence, it can still be used as a conventional large-eddy simulation or cloud-resolving model over limited domains. The latitude-longitude grid allows gSAM to run both globally and over very large regional domains for which a Cartesian grid is not sufficiently accurate because of the Earth's curvature.

gSAM is unique among GSRMs in using an anelastic dynamical core with a single reference profile, like past versions of SAM. However, the anelastic equations used in gSAM, which follow Pauluis (2008), differ from most other anelastic models in ways that are helpful for global modeling. Buoyancy in gSAM is based on the absolute temperature, not the potential temperature, and the prognostic thermodynamic equation is based on a moist form of the static energy, rather than potential temperature; these modifications are convenient for microphysical parameterization. The thermodynamic equation also includes the vertical flux of buoyancy (Pauluis, 2008). The resulting system is shown to conserve the global integral of the sum of the kinetic, thermodynamic, and potential energies. For quasi-hydrostatic flows, the anelastic system in gSAM is isomorphic to the primitive equations in pressure coordinates, but with the globally-uniform reference pressure (which is a known function of height) in gSAM playing the role of actual pressure. Therefore, to preserve geophysically important relationships such as geostrophic and hydrostatic balance, initialization of gSAM by external data should be done by mapping horizontal velocity, temperature and other data in pressure coordinates to the reference pressures of each grid level, instead of using a direct column-by-column interpolation of the data to height coordinates. If this is done in a standard gradient-wind balance test, gSAM can exactly maintain steady zonally symmetric baroclinic flows that have been specified in pressure coordinates. This isomorphism helps rationalize how gSAM can simulate realistic global temperature and wind distributions even though assumptions underlying the anelastic approximation, such as the smallness of horizontal pressure perturbations, become shaky on global scales.

Several tests of gSAM's accuracy in simulating global-scale flows without topography were presented. Results of a standard baroclinic-wave test compare quite well to other models' results. In a Held-Suarez test, the mean general circulation agrees well with results from the Community Atmosphere Model with Eulerian dynamical core at similar horizontal grid resolution. In a barotropic equatorial

Rossby-Haurwitz wave test, gSAM accurately maintains the expected shape and magnitude of the wave very well and propagates the wave in the westward direction at a speed very close to the theoretically derived value.

The treatment of topography in gSAM is novel among global atmospheric models, which generally use terrain-following coordinates. gSAM uses altitude as the vertical coordinate. This considerably simplifies the discretized fluid transport equations, but it means that some grid points lie within regions of elevated terrain. The surface boundary condition is enforced using a type of immersed boundary method, the Quasi-Solid Body Method (QSBM), in which the flow velocity in grid cells inside prescribed terrain is stagnated using "instantaneous" relaxation to zero. The QSBM method works well, as demonstrated by two tests: linear non-hydrostatic flow over an idealized mountain range and a global simulation hydrostatic Rossby waves induced by a large circular mountain. Starting with a no-topography model version, implementing the QSBM requires minimal code changes and no algorithmic change to the sophisticated multigrid anelastic Poisson solver used in gSAM.

Several results were presented from a real-Earth simulation performed for the DYAMOND-Winter project. We compared several important fields with ERA-5 reanalysis, such as precipitation, surface latent heat flux and top-of-atmosphere OLR and solar radiation, averaged over January 21-25, 2020. Despite several notable biases, the gSAM results track the reanalysis well over this relatively short period.

We also presented results of a hindcast of Hurricane Irma in 2017. We used a 17-km grid to perform a 10-member ensemble runs and high-resolution 4-km for a single deterministic run initialized from the ERA5 data five days before Irma's landfall in Florida. The ensemble predicts the hurricane track quite well but considerably underpredicts the hurricane intensity just before landfall. In contrast, the deterministic run predicts an intensity similar to that observed, both in minimum surface pressure and maximum surface wind.

Our future research with gSAM will be conducted on multiple fronts. We will continue working on improving the accuracy of simulations around the poles and on achieving optimal computational performance on evolving high-performance computing architectures. We plan to run gSAM in weather-nudged mode, forced by reanalysis data, with different microphysical packages, to improve representation of clouds and radiation and better understand how different cloud microphysics parameterizations affect the results. We will evaluate the simulation of the diurnal cycle over land, especially of precipitation, and work on further improvement of the Simplified Land Model and especially its treatment of snow cover.

We will further evaluate the suitability of gSAM (including regional versions that can be used with finer grids) for forecasting extreme weather events in present and future climates.

Acknowledgements We thank Prof. Xiangmin Jiao, and his students Cao Lu and Oliver Yang from the Dept. of Applied Mathematics and Statistics and the Institute for Advanced Computational Science at Stony Brook University for their help in developing and implementing an efficient GMG pressure solver in gSAM. Marat Khairoutdinov was supported by the NSF grant AGS-1418309 to Stony Brook University and by subaward to NSF grant AGS-1660604 to University of Washington. Chris Bretherton and Peter Blossey were supported by NSF grants AGS-1660604 and OISE- 1743753. We would like to acknowledge high-performance computing support from Cheyenne (doi:10.5065/D6RX99HX) provided by NCAR's Computational and Information Systems Laboratory, sponsored by the NSF. The data from dynamical core tests is accessible through NCAR Campaign Storage via Globus. The DYAMOND data is archived by the German Climate Computing Centre (DKRZ) through the ESiWACE project (https://www.esiwace.eu/services/dyamond).

References

Adcroft, A., Hill, C., Marshall, J., 1997: Representation of topography by shaved cells in a height coordinate ocean model. *Mon. Wea. Rev. 125*, 2293–2315

Asaithambi R., and K. Mahesh, 2017: A note on a conservative finite volume approach to address numerical stiffness in polar meshes. *J. Comp. Phys*., *341*, 377-385.

Atlas, R., C. S. Bretherton, M. F. Khairoutdinov, P. N. Blossey, 2021: Hallett-Mossop rime splintering dims the Southern Ocean: New insight from global cloud-resolving simulations. *AGU Advances*, in review, doi:10.1002/essoar.10507321.2.

Bretherton, C.S., and M. Khairoutdinov, 2015: Convective self-aggregation feedbacks in near-global cloud-resolving simulations of an aquaplanet. *J. Adv. Model. Earth Syst*., **7**, 1765-1787, doi:10.1002/2015MS000499

Chan, S. T., and Leach, M. J., 2007: A validation of FEM3MP with Joint Urban 2003 data. *J. Appl. Meteor. and Clim.*, *12*, 2127–2146.

Collins, W. D., and Coauthors, 2006: The formulation and atmospheric simulation of the Community Atmosphere Model version 3 (CAM3). *J. Climate*, *19*, 2144–2161.

Durran, D. R. (1991). The third-order Adams-Bashforth method: An attractive alternative to leapfrog time differencing. *Mon. Wea. Rev*, *119*, 702-720.

Judt, F. D., and 25 others, 2021: Tropical Cyclones in Global Storm-Resolving Models, *J. Meteor. Soc. Japan*. Ser. II, No. 3, 579-602. doi:10.2151/jmsj.2021-029

Fiedler, B. H., and R. J. Trapp, 1993: A Fast Dynamic Grid Adaption Scheme for Meteorological Flows. *Mon. Wea. Rev*., *121*, 2879-2888.

Held, I. M., and M. J. Suarez, 1994: A proposal for the intercomparison of the dynamical cores of atmospheric general circulation models, *Bull. Amer. Meteorol. Soc*., *75*, 1825–1830.

Hurrell, J. W.; M. M. Holland; P. R. Gent (2013). "The Community Earth System Model: A Framework for Collaborative Research". *Bull. Amer. Meteorol. Soc*., *94*, 1339–1360.

Iacono, M. J., Delamere, J. S., Mlawer, E. J., Shephard, M. W., Clough, S. A., and Collins, W. D. (2008), Radiative forcing by long-lived greenhouse gases: Calculations with the AER radiative transfer models, *J. Geophys. Res.*, *113*, D13103, doi:10.1029/2008JD009944.

IPCC 2013: Climate Change 2013: The Physical Science Basis. Contribution of Working Group I to the Fifth Assessment Report of the Intergovernmental Panel on Climate Change. Cambridge University Press. Retrieved from https://www.ipcc.ch/report/ar5/wg1/, doi:10.1017/CBO9781107415324

IPCC, 2021: AR6 Climate Change 2021: The Physical Science Basis. https://www.ipcc.ch/report/ar6/wg1/

Jablonowski C, and D.L. Williamson, 2006. A baroclinic instability test case for atmospheric model dynamical cores. *Q. J. R. Meteorol. Soc*., *132*, 2943–2975.

Jablonowski, C., P.H. Lauritzen, M.A. Taylor, R.D. Nair, 2008: Idealized test cases for the dynamical cores of atmospheric general circulation models: a proposal for the NCAR ASP 2008 summer colloquium, Technical Report. http://www-personal.umich.edu/~cjablono/NCAR_ASP_2008_idealized_testcases_29May08.pdf

Khairoutdinov, M. F., and D.A. Randall, 2003: Cloud-resolving modeling of the ARM summer 1997 IOP: Model formulation, results, uncertainties and sensitivities. *J. Atmos. Sci*., *60*, 607-625.

Khairoutdinov, M., and K. Emanuel, 2018: Intraseasonal variability in a cloud-permitting near-global equatorial aqua-planet model. *J. Atmos. Sci.*, *75*, 4337-4355, doi:10.1175/jas-d-18-0152.1

Khairoutdinov, M. F., A. M. Vogelmann, and K. Lamer, 2022: Adding building resolving capabilities into the System for Atmospheric Modeling using the Quasi-Solid Box Method. *J. Adv. Model. Earth Syst*., submitted. Preprint: doi:10.1002/essoar.10509425.1

Klemp, J. B., W. C. Skamarock, and S.-H. Park, 2015: Idealized global nonhydrostatic atmospheric test cases on a reduced-radius sphere, *J. Adv. Model. Earth Syst*., *7*, 1155–1177, doi:10.1002/2015MS000435.

Kurowski, M. J., W. W. Grabowski, and P. K. Smolarkiewicz, 2013: Toward multiscale simulation of moist flows with soundproof equations, *J. Atmos. Sci.*, *70*, 3995-4011. https://doi.org/10.1175/JAS-D-13-024.1

Kurowski, M. J., W.W. Grabowski, and P. K. Smorarkiewicz, 2015: Anelastic and compressible simulation of moist dynamics at Planetary Scales. *J. Atmos. Sci*., *72*, 3975-3995.

Lee, J. K., and M. Khairoutdinov, 2015: Simplified Land Model (SLM) for use in cloud resolving models: Formulation and evaluation. *J. Adv. Model. Earth Syst*., *7*, doi:10.1002/2014MS000419

Lipps, F., and. R. Hemler, 1982: A scale analysis of deep moist convection and some related numerical calculations. *J. Atmos.Sci*., 39, 2192-2210.

Lu, C, 2016: Efficient Iterative and Multigrid Solvers with Applications, Ph.D. Dissertation, Stony Brook University Thesis and Dissertations Collection, http://hdl.handle.net/11401/77232

774 Morrison, H. and J. A. Milbrandt, 2015: Parameterization of Cloud Microphysics Based on the
775 Prediction of Bulk Ice Particle Properties. Part I: Scheme Description and Idealized Tests, *J. Atmos.*
776 *Sci.*, *72*, 287–311, https://doi.org/10.1175/JAS-D-14-0065.1
777 Morrison, H., J. A. Curry, and V. I. Khvorostyanov, 2005: A new double-moment microphysics
778 parameterization for application in cloud and climate models. Part I: Description. *J. Atmos.*
779 *Sci.*, *62*, 1665–1677, https://doi.org/10.1175/JAS3446.1.
780 Narenpitak, P., C. S. Bretherton, and M. Khairoutdinov, 2017: Cloud and circulation feedbacks in a
781 near-global aquaplanet cloud-resolving model. *J. Adv. Model. Earth Syst*, *9*, 1069-1090,
782 doi:10.1002/2016MS000872.
783 Narenpitak P., C. S. Bretherton, and M. F. Khairoutdinov, (2020). The role of multiscale interaction in
784 tropical cyclogenesis and its predictability in near-global aquaplanet cloud-resolving simulations. *J*
785 *Atmos Sci.*, *77*, 2847-2863
786 Nastrom, G.D., and Gage, K. S., 1985: A climatology of atmospheric wavenumber spectra of wind and
787 temperature observed by commercial aircraft. *J. Atmos. Sci.*, *42*, 950-960.
788 Pauluis O., 2008: Thermodynamic consistency of the anelastic approximation for a moist atmosphere. *J.*
789 *Atmos. Sci.*, *65*, 2719-2729
790 Randall, D., M. Khairoutdinov, A. Arakawa, and W. Grabowski, 2003: Breaking the cloud
791 parameterization deadlock. *Bull. Amer. Meteorol Soc, 84*, 1547–1564.
792 Satoh, M., B. Stevens, F. Judt, M. Khairoutdinov, S.-J. Lin, W. Putman, and P. Dueben, 2019: Global
793 cloud-resolving models, *Curr. Clim. Change Rep.*, https://doi.org/10.1007/s40641-019-00131-0
794 Schär, C., D. Leuenberger, O. Fuhrer, D. Lüthi, and C. Girard (2002). A new terrain-following vertical
795 coordinate formulation for atmospheric prediction models. *Mon. Wea. Rev. 130*, 2459–2480.
796 Smolarkiewicz, P.K., 2006: Multidimensional positive definite advection transport algorithm: an
797 overview, *Int. J. Numer. Methods Fluids*. *50*, 1123–1144.
798 Smolarkiewicz, P. K., Sharman, R., Weil, J., Perry, S. G., Heist, D., & Bowker, G. (2007). Building
799 resolving large-eddy simulations and comparison with wind tunnel experiments. *Journal of*
800 *Computational Physics*, *227*, 633–653.
801 Stevens B, and S. Bony, 2013: What are climate models missing? *Science*, *340*, 1053–1054.
802 Stevens, B., Satoh, M., Auger, L., Biercamp, J., Bretherton, C. S., Chen, X., P. Dueben, F. Judt, M.
803 Khairoutdinov, D. Klocke, C. Kodama, L. Kornblueh, S.-J. Lin, W. Putman, R. Shibuya, P.
804 Neumann, N. Roeber, B. Vanniere, P.-L. Vidale, N. Wedi, L. Zhou (2019). DYAMOND: The

DYnamics of the Atmospheric general circulation MOdeled on Non-hydrostatic Domains. *J. Meteor. Soc. Japan.,6,* https://doi.org/10.1186/s40645-019-0304-z

Thompson, G., P. R. Field, R.M. Rasmussen, and W.D. Hall, 2008: Explicit forecasts of winter precipitation using an improved bulk microphysics scheme. Part II: Implementation of a new snow parameterization. *Mon. Wea. Rev.*, *136*, 5095–5115, https://doi.org/10.1175/2008MWR2387.1.

Tomita H, and M. Satoh, 2004: A new dynamical framework of nonhydrostatic global model using the icosahedral grid. *Fluid Dyn Res*., *34*, 357–400.

Ullrich, P. A., C. Jablonowski, J. Kent, P. H. Lauritzen, R. D. Nair, and M. A. Taylor (2012), Dynamical Core Model Intercomparison Project. (DCMIP) Test Case Document, Earth System CoG. [http://www-personal.umich.edu/~cjablono/DCMIP-2012_TestCaseDocument_v1.7.pdf]

Ullrich, P. A., and C. Jablonowski, 2012: MCore: A non-hydrostatic atmospheric dynamical core utilizing high-order finite-volume methods, *J. Comp. Phys*, *231*, 5978-5108.

Williamson, D.L., J. Drake, J. Hack, R. Jakob, and P. Swarztrauber, 1992: A standard test set for numerical approximations to the shallow water equations in spherical geometry, *J. Comp. Phys*. *102*, 211–224

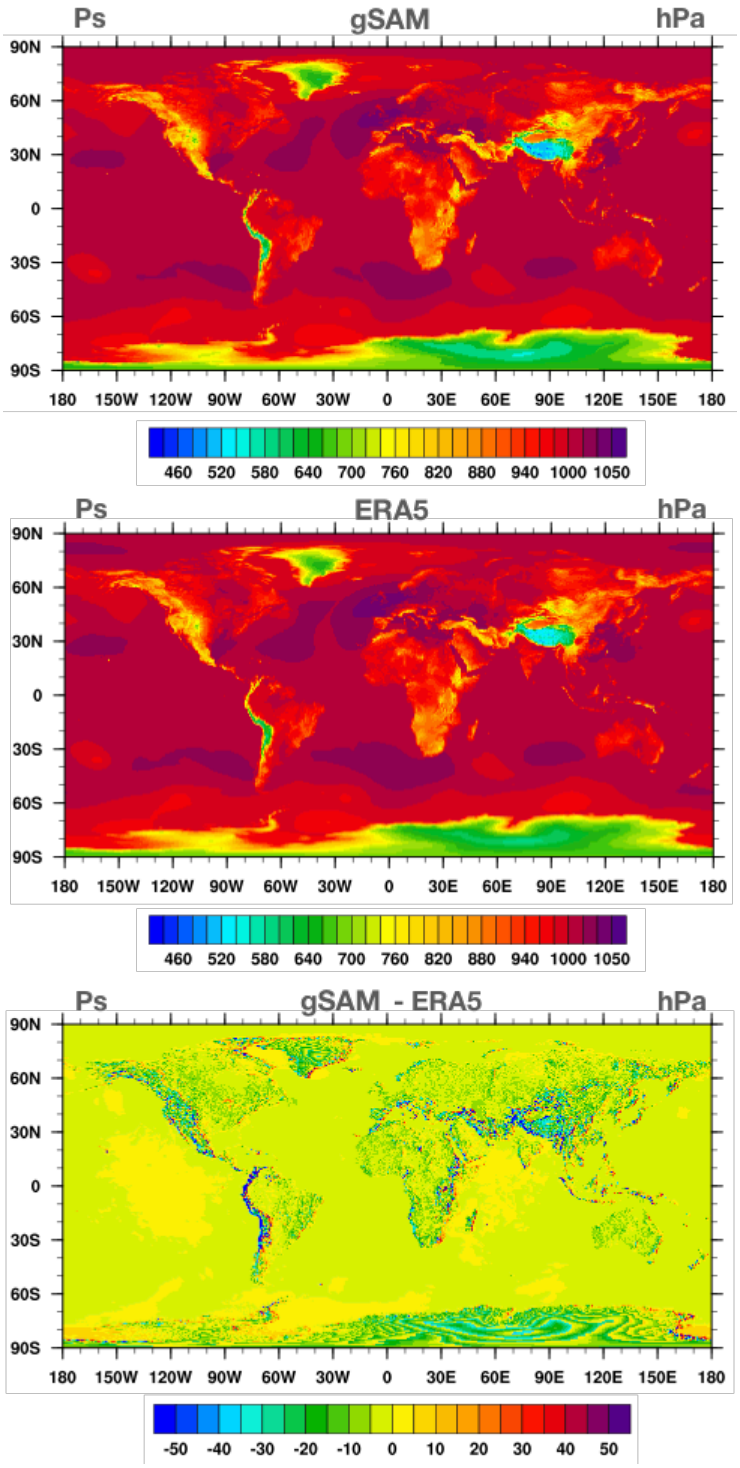

823

824 **Figure 1.** Comparison of surface pressure computed by gSAM (top) and ERA5 reanalysis (middle),
825 along with their difference (bottom) after one-hour simulation starting at 00Z on January 2020.

826

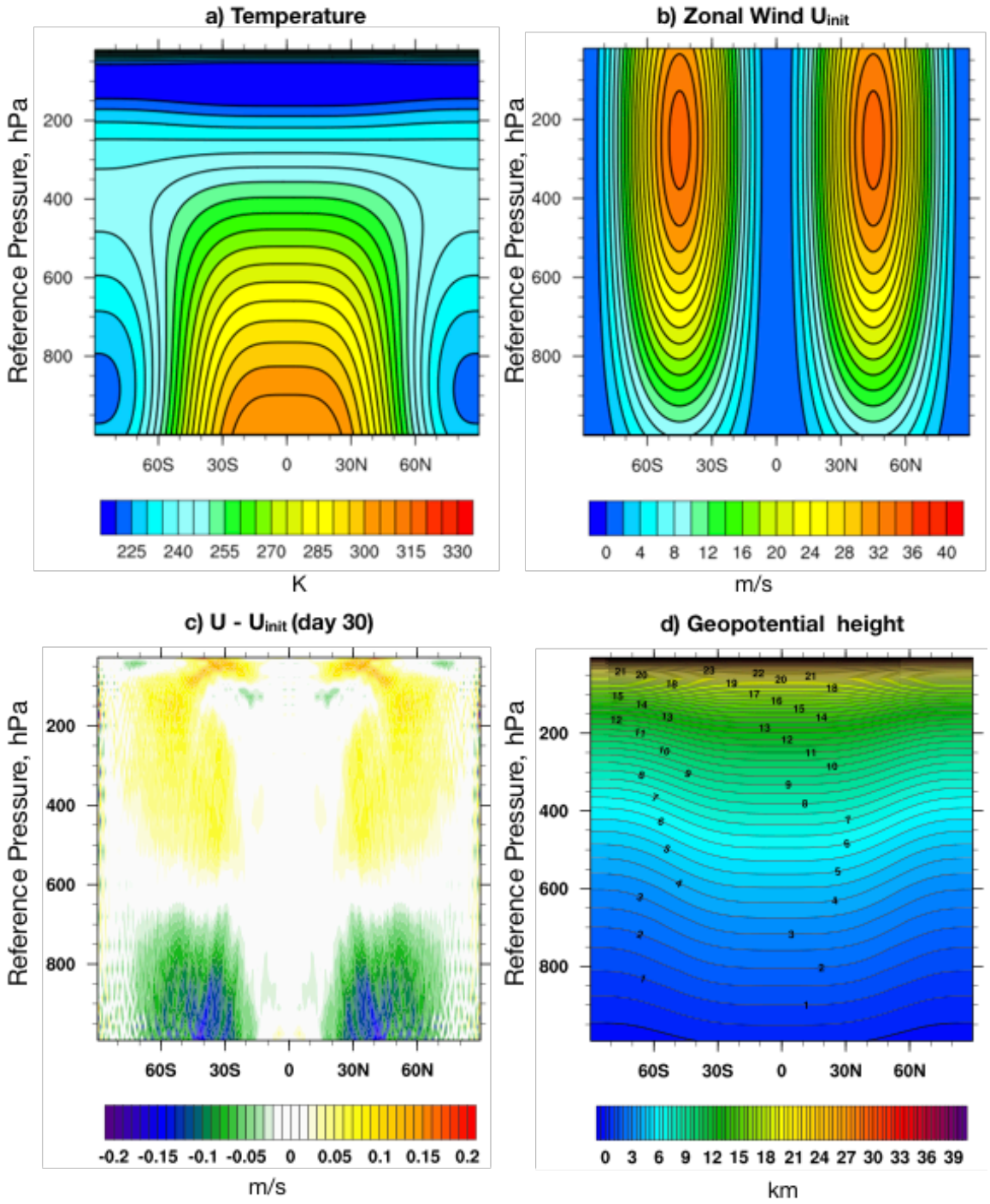

Figure 2. Initial a) temperature, b) zonal wind, c) pressure, d) geopotential height (zero level is shown by thicker isoline), and deviation from initial e) zonal and f) meridional wind after 30 days of SAM integration in the steady state test.

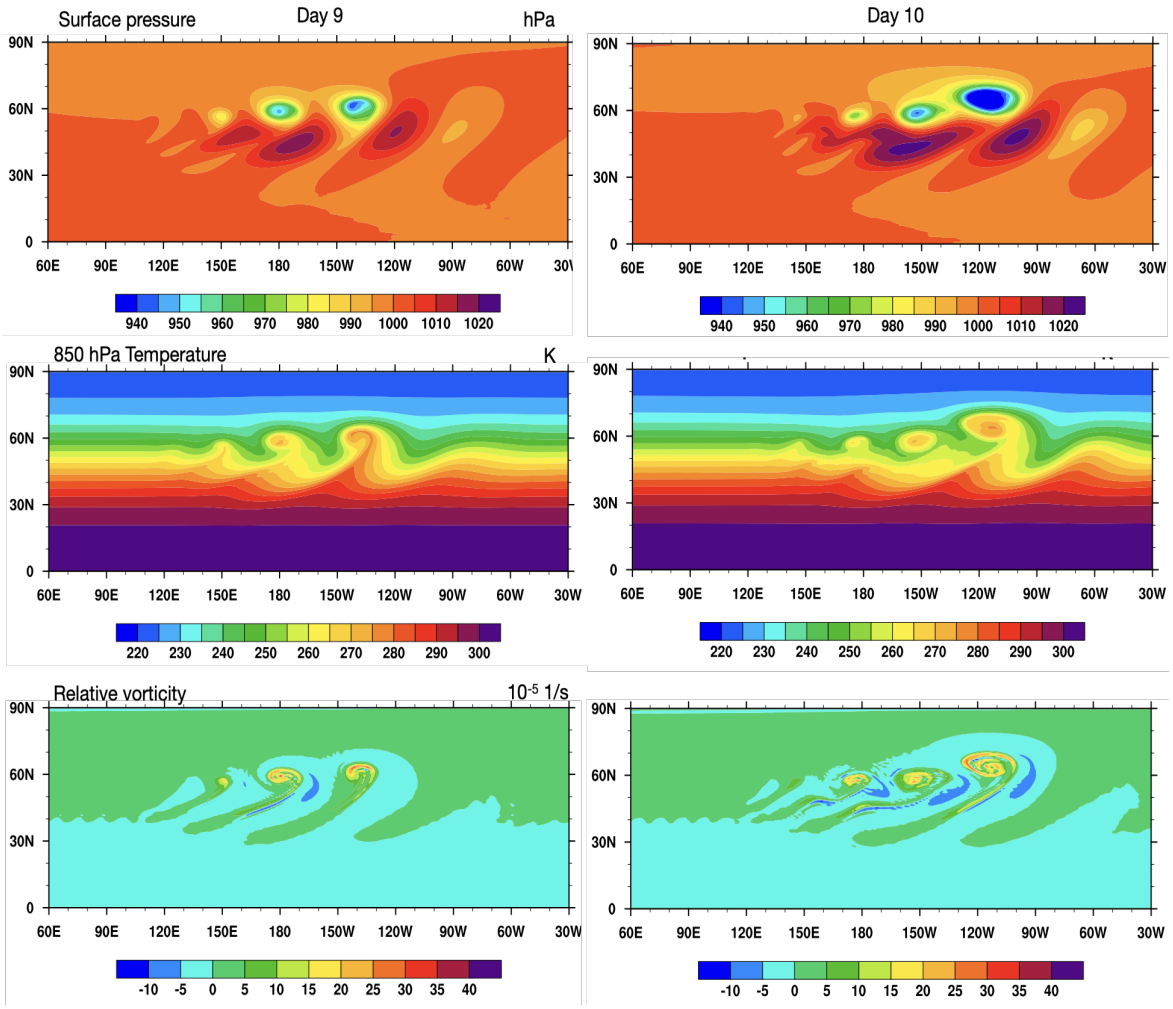

Figure 3. (top) Surface pressure, (middle) temperature at 850 hPa, and (bottom) relative vorticity at 850 hPa at (left) day 9 and (right) day 10 of the evolution of baroclinically unstable wave.

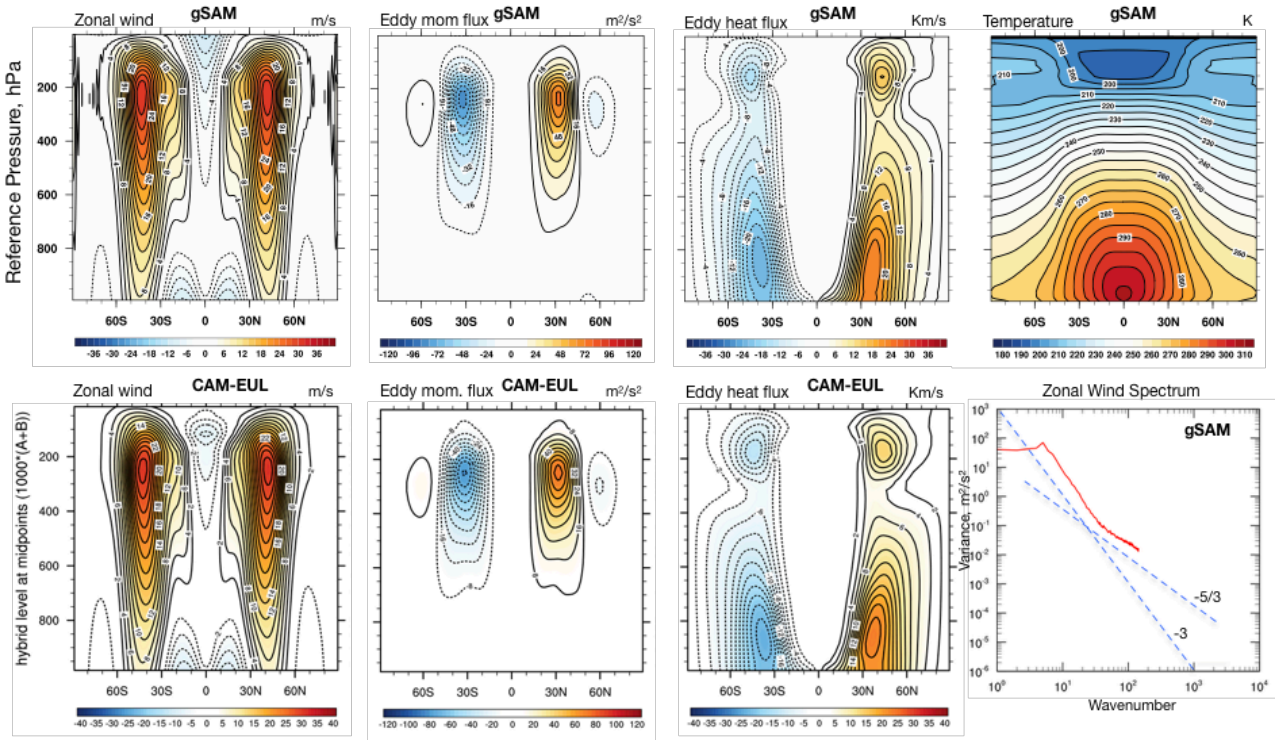

Figure 4. 1000-day mean climatology from the Held-Suarez test for various fields for gSAM (top panels) and CAM-EUL (three left bottom panels). The right-bottom panel shows the mid-latitude zonal-wind variance spectrum for gSAM. The panels for CAM-EUL have been adopted from the CESM website https://www.cesm.ucar.edu/models/simpler-models/held-suarez.html .

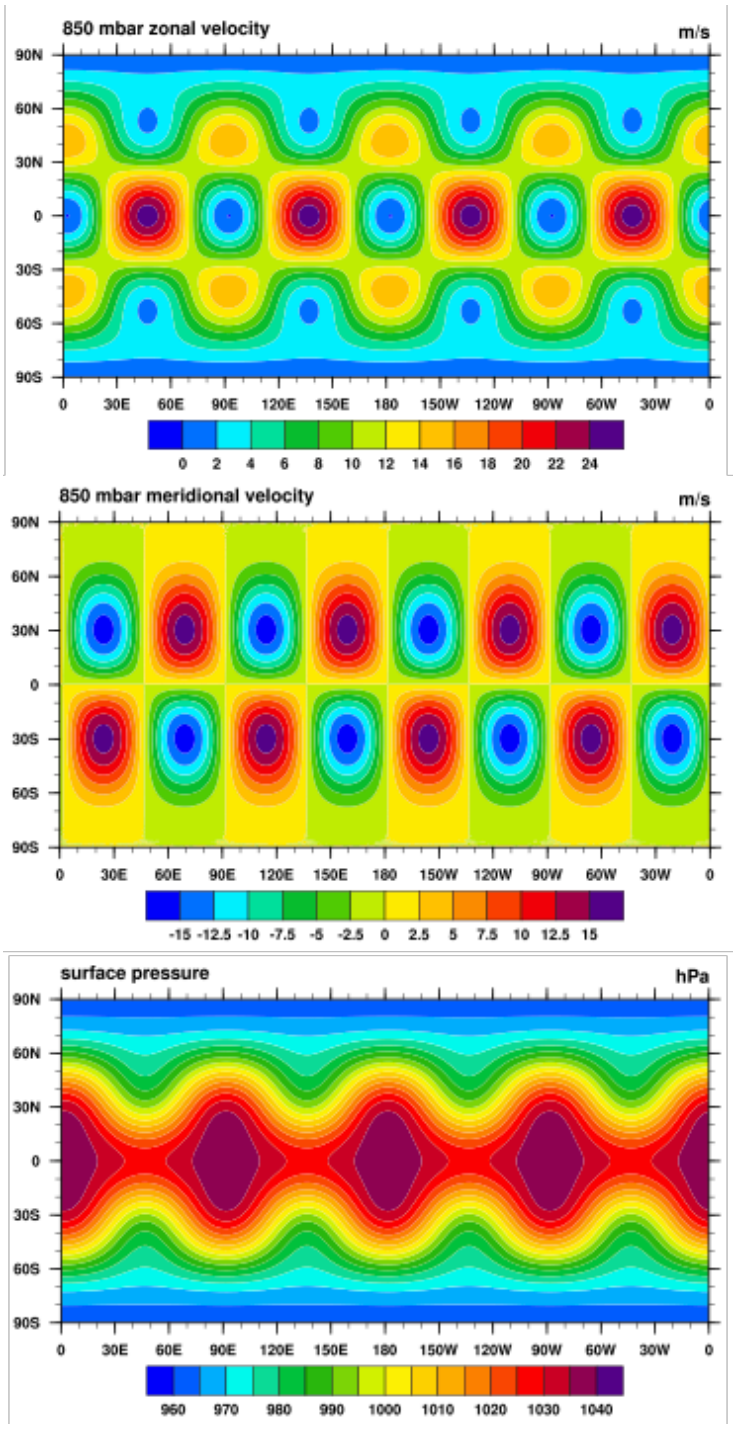

Figure 5. The snapshot of the velocity components at 850 hPa levels as well as surface pressure after 24 days of evolution of the Rossby-Haurwotz wave.

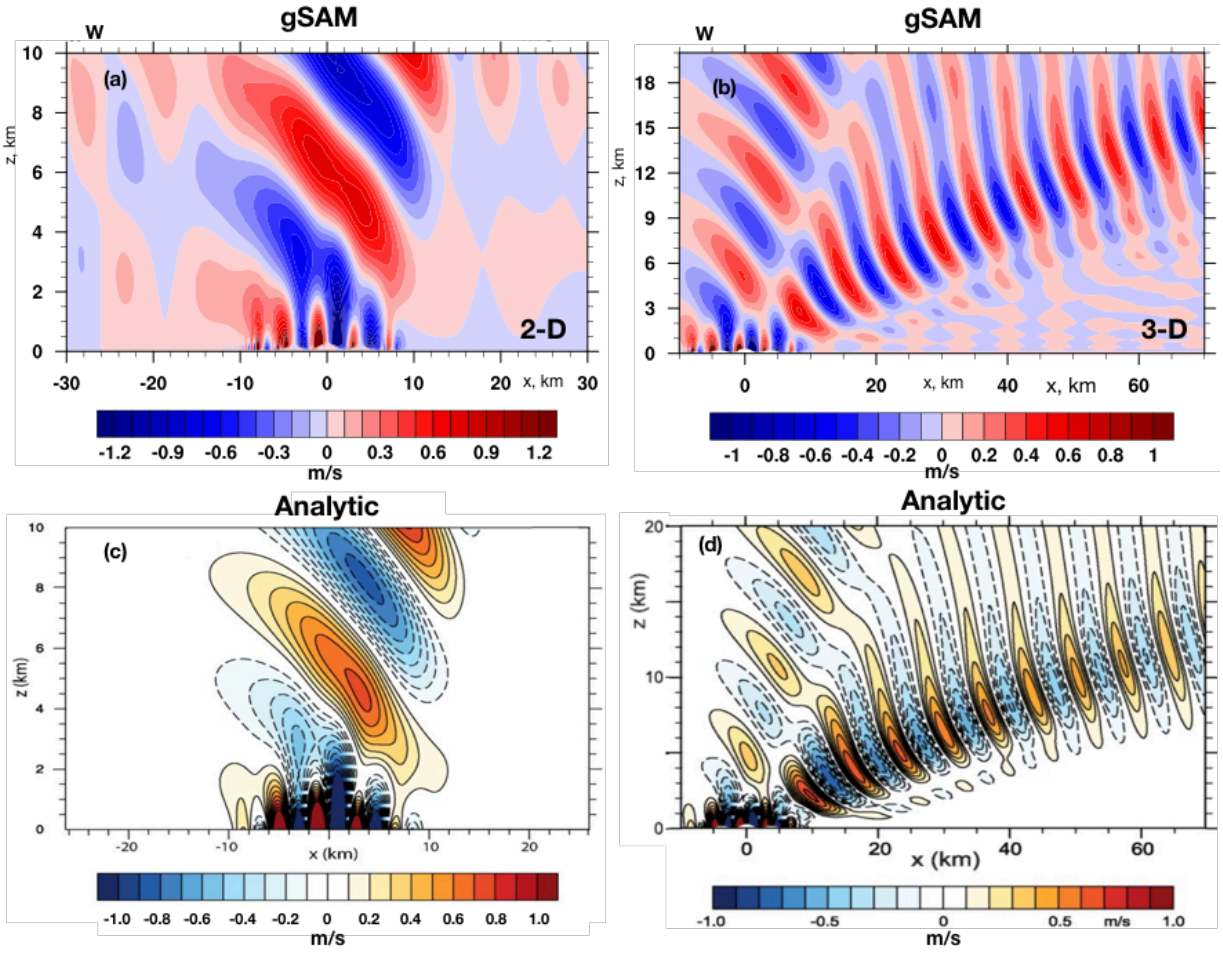

Figure 6. Vertical cross section of vertical velocity over a) 2-D and b) 3-D Schär-type mountain ranges. The plots c) and d) for corresponding analytical linear solutions are adopted from Klemp et al (2015).

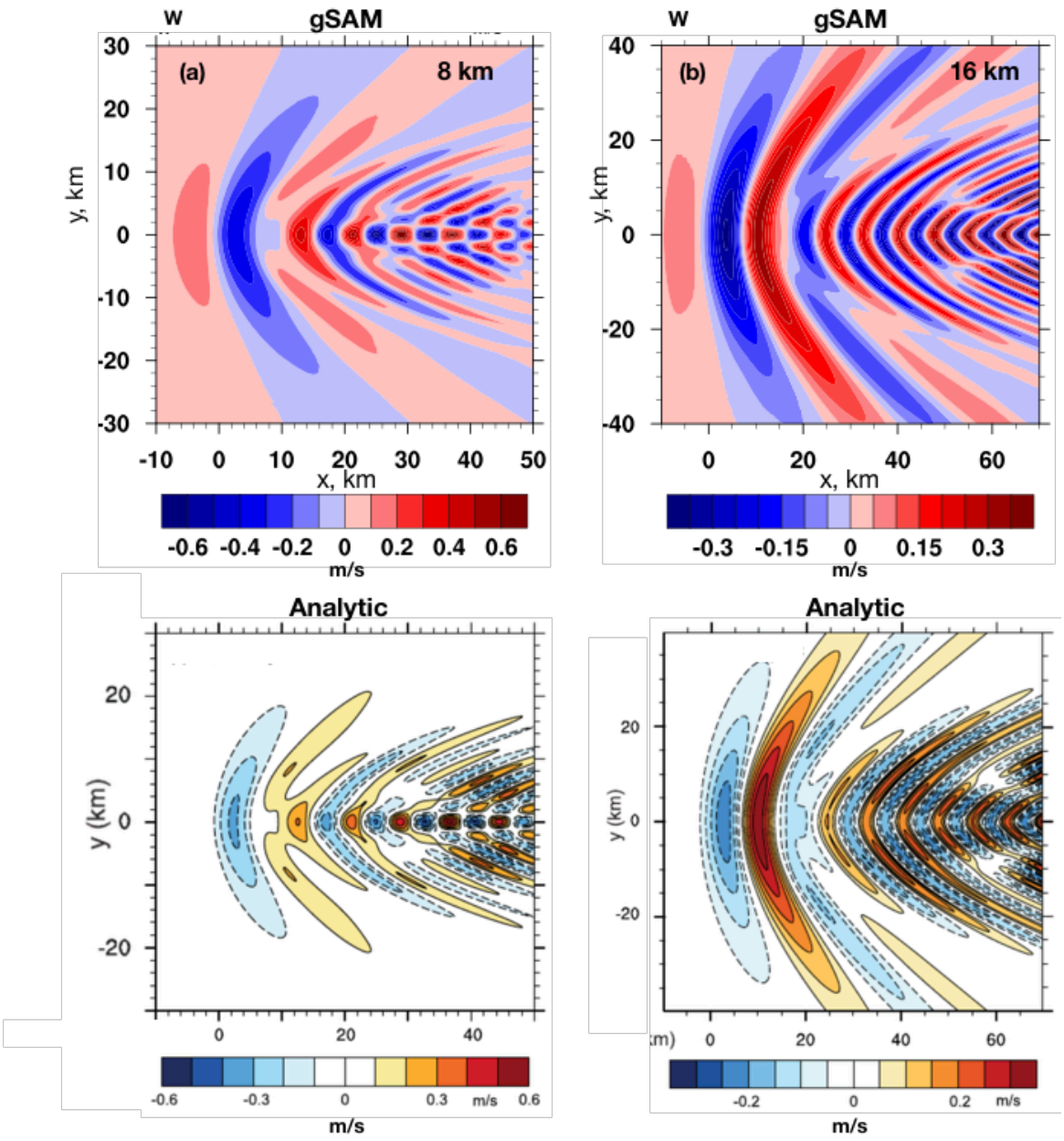

Figure 7. Horizontal cross section of vertical velocity over 3-D Schär-type mountain ranges at c) 8 km and d) 16 km height. The plots c) and d) for corresponding analytical linear solutions are adopted from Klemp et al (2015).

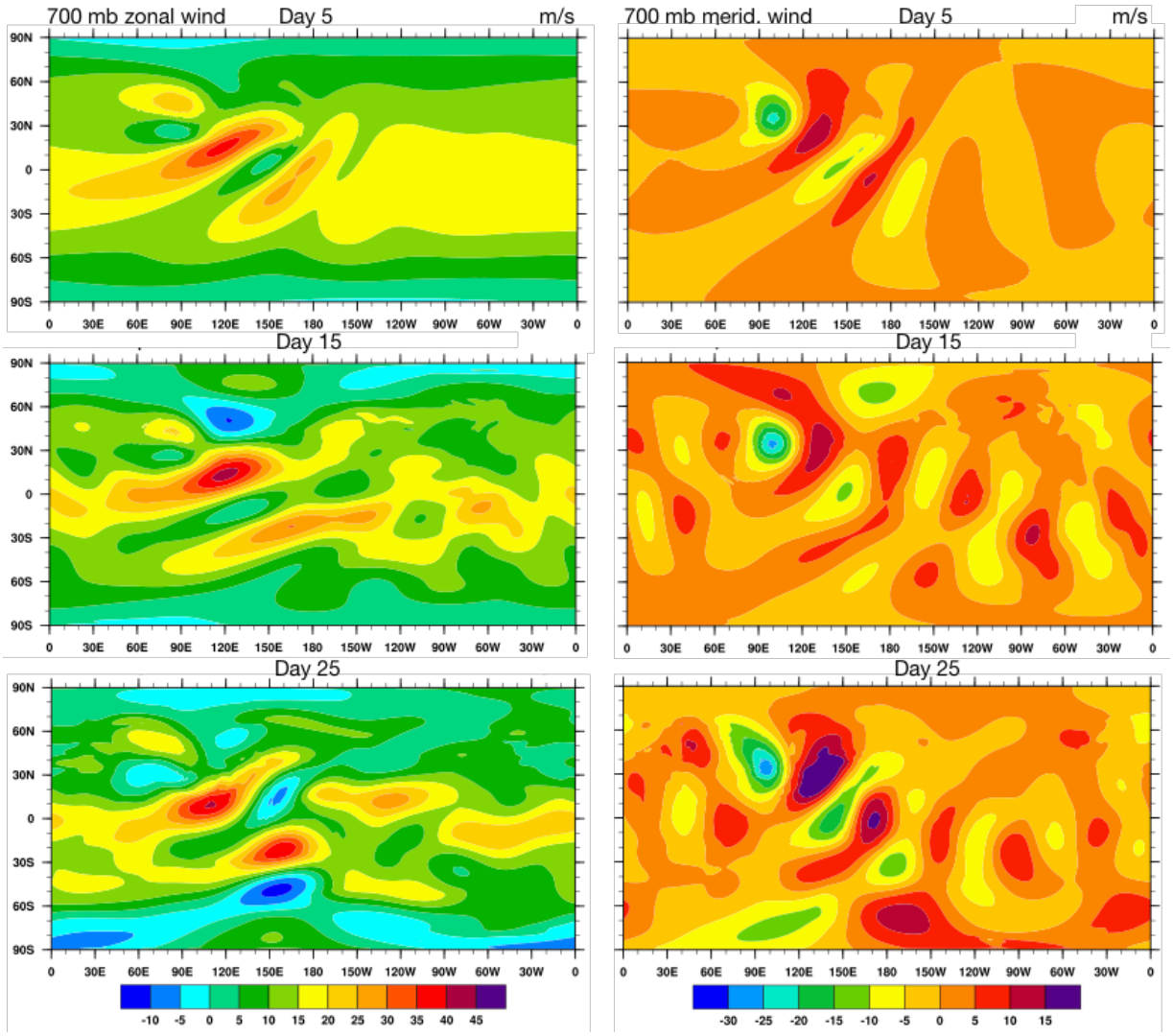

Figure 8. The snapshots of wind components at 700 mb at (top) day 5, (middle) day 15, and (bottom) day 25 of the Rossby wave-train induced by a circular mountain. The center of the 2-km heigh and 1500-km wide bell-shaped mountain is at 90°E and 30°N.

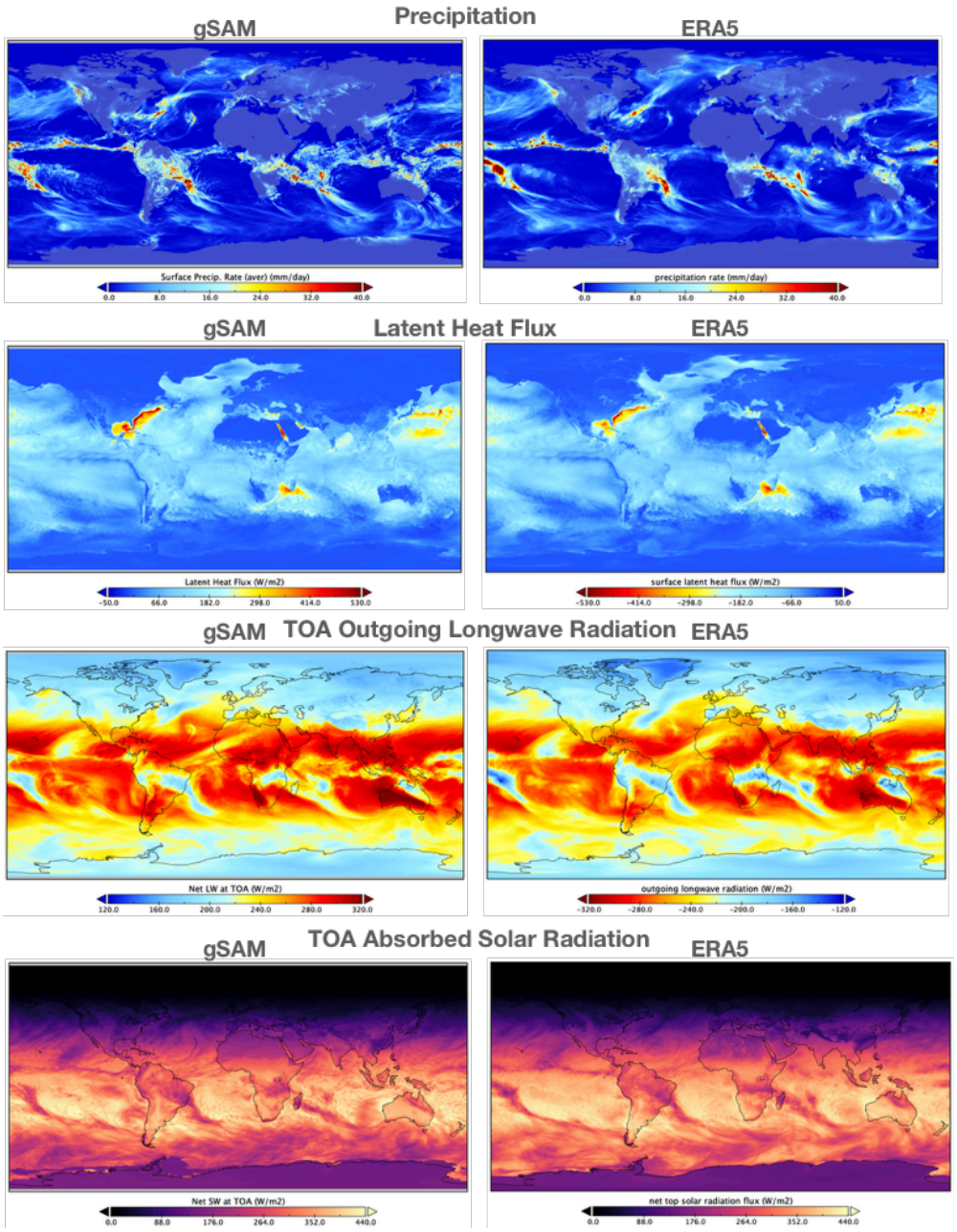

Figure 9. The 5-day (00Z Jan 21 – 00Z Jan 26, 2020) average precipitation rate, latent heat flux, TOA outgoing longwave and absorbed solar radiative fluxes for gSAM (left panels) and ERA4 (right panels).

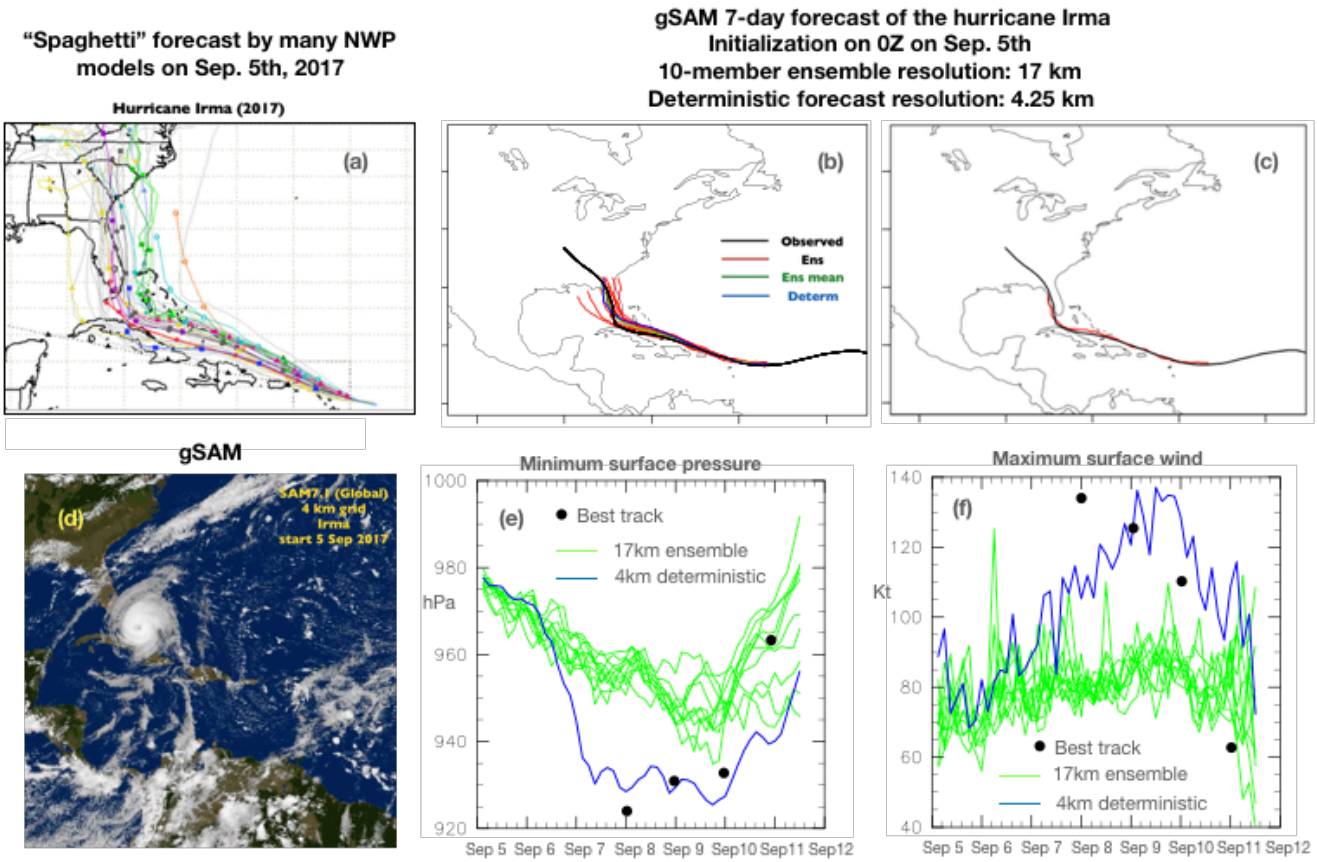

Figure 10. (a) "Spaghetti" forecast from NWP models as of September 5; (b) tracks predicted by gSAM: 10-member ensemble (red) and ensemble mean (green), deterministic (blue), and best-track (black); (c) track of one of the "lucky" ensemble members; (d) simulated satellite view of Irma using predicted fields from gSAM; e) minimum surface pressure and (f) maximum surface wind for ensemble members (green) and deterministic run (blue). Best-track data are denoted by black dots.